

Denoising Functional Maps: Diffusion Models for Shape Correspondence

Aleksei Zhuravlev¹ Zorah Löhner¹ Vladislav Golyanik²
¹University of Bonn ²MPI for Informatics, SIC

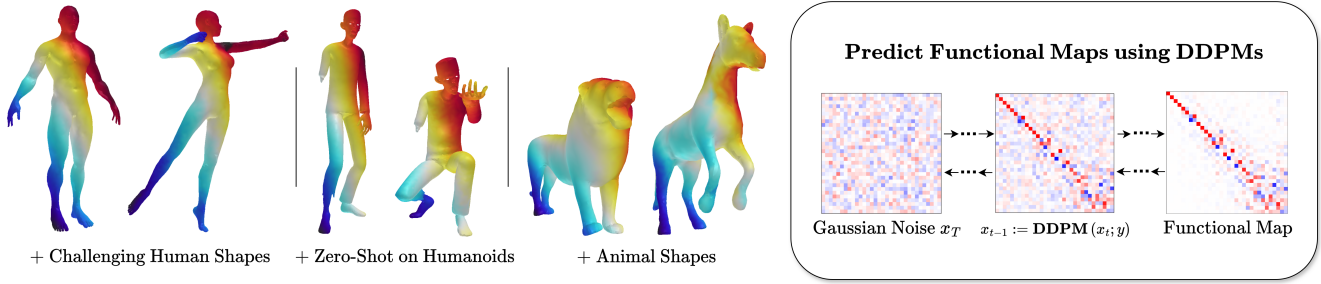


Figure 1. We propose DenoisFM, a novel framework for predicting shape correspondences in the form of functional maps using denoising diffusion models. (Left:) Challenging examples our method can handle, with color-coded correspondences. (Right:) By sequentially denoising samples of random noise, the diffusion model can predict the correct functional map between a pair of shapes.

Abstract

Estimating correspondences between pairs of deformable shapes remains a challenging problem. Despite substantial progress, existing methods lack broad generalization capabilities and require category-specific training data. To address these limitations, we propose a fundamentally new approach to shape correspondence based on denoising diffusion models. In our method, a diffusion model learns to directly predict the functional map, a low-dimensional representation of a point-wise map between shapes. We use a large dataset of synthetic human meshes for training and employ two steps to reduce the number of functional maps that need to be learned. First, the maps refer to a template rather than shape pairs. Second, the functional map is defined in a basis of eigenvectors of the Laplacian, which is not unique due to sign ambiguity. Therefore, we introduce an unsupervised approach to select a specific basis by correcting the signs of eigenvectors based on surface features. Our approach achieves competitive performance on standard human datasets, meshes with anisotropic connectivity, non-isometric humanoid shapes, as well as animals compared to existing descriptor-based and large-scale shape deformation methods. The source code and the datasets can be found on our project page: <https://alekseizhuravlev.github.io/denoising-functional-maps/>.

1. Introduction

A long-standing problem in computer graphics and vision is to find corresponding points in a pair of 3D shapes [9, 11, 19, 42, 49, 64, 69]. The point map can then be used for texture [14], segmentation [63] and deformation transfer [68], statistical shape analysis [13], and construction of parametric models [37, 55]. A popular approach to solving the correspondence problem involves the functional map framework [49], which represents the correspondence as a small matrix that maps the eigenfunctions of the Laplace operator on each shape. This representation is compact and allows to enforce constraints on the correspondences, such as bijectivity or area preservation. The functional map framework has been extended in numerous works, such as matching shapes with partiality [4, 58], analyzing the properties of shape collections [13] or improving accuracy through iterative refinement [19, 44, 57].

Previous functional map approaches focused on using small datasets, rarely exceeding a hundred unique shapes. This favored training models with lightweight architectures that could learn as much as possible with limited data. At the same time, they would be highly category-specific, e.g. suitable for a particular class of human shapes but lacking generalization to humanoids. To develop a unified model that is applicable to various tasks, we draw attention to denoising diffusion models [25, 66, 67], which have impressive generalization ability when trained on large amounts of data. In this paper, we apply this approach to correspondence estimation using functional maps.

Based on the idea of sequentially denoising im-

ages blurred with Gaussian noise, diffusion models have achieved unprecedented performance in high-fidelity, diverse, and controllable image synthesis [53]. The scalable U-Net architecture [60] allows them to be trained on large datasets with hundreds of thousands of high-resolution images. The application of diffusion models to shape matching has been limited so far, mainly focusing on feature extraction from pre-trained foundational models [1, 17]. Interestingly, functional maps appear well-suited to bridge diffusion models and shape correspondence. They are small-sized single-channel matrices, making standard architectures developed for images readily applicable to them. Large amounts of shape data for training are then available through parametric models such as SMPL [37], an approach that has already been used for matching tasks [23, 72] and is also suitable for diffusion models.

In this work, we present Denoising Functional Maps (DenoisFM), an approach to directly predict the functional map between shapes using a denoising diffusion model; see Fig. 1 for the overview. For training, we create a large dataset of functional maps between $2.3 \cdot 10^5$ human shapes from the SURREAL dataset [73] and a template shape. Using template-wise maps instead of pair-wise ones allows to reduce the complexity of training and inference. The conditioning information is inferred directly from the geometric shape structure. Additionally, we propose to exploit the probabilistic nature of diffusion models by predicting several initial maps instead of a single one, and selecting the best map based on the Dirichlet energy [52].

An important property of functional maps is that they are defined in the basis of the first n eigenvectors of the Laplacian operator for each shape. The basis is not unique due to the sign ambiguity of the eigenvectors, and there are potentially 2^n possible basis combinations for each shape. To address this problem, we propose an unsupervised approach which selects the signs of the basis vectors using per-vertex features extracted in an unsupervised way (see Sec. 3.2). This reduces the number of possible functional maps between shapes, further lowering the training complexity.

Contributions. Overall, the technical contributions of this paper can be summarized as follows:

- DenoisFM, a fundamentally new approach to shape correspondence estimation based on predicting functional maps using denoising diffusion models;
- An unsupervised method to address the sign ambiguity of eigenvectors of the Laplacian, which reduces the complexity of the prediction problem.

Our model performs on par with existing shape matching methods on human benchmark datasets, achieves generalization to non-isometric humanoid shapes without learning on them, and is also applicable to animal shapes. See our project page for the source code and the datasets of functional maps used to train our models.

2. Related Work

Shape Correspondence Estimation. Learning-based shape correspondence methods can be roughly divided into two categories: first, approaches that predict point-wise descriptors suitable for computing functional maps [49, 50], a low-rank representation of the point-wise correspondence in Laplace–Beltrami eigenbasis; second, deformation-based methods that directly align input shapes and typically require much larger training datasets than descriptor-based methods.

In the standard functional map pipeline, point-wise descriptor functions that encode the surface geometry are first computed on each shape [5, 9, 71], and then the functional map is estimated using the descriptors in a least-squares optimization. With the advent of deep learning, network architectures were introduced to learn descriptor functions directly from the data [35, 65]. While the initial methods were supervised [15, 35], recent works estimate the descriptors in an unsupervised manner [11, 62]. Most shape matching datasets consist of fewer than a hundred unique meshes and focus on a specific category of shapes [3, 7, 40, 43]. Therefore, the most effective descriptor-based models use lightweight architectures to infer as much geometric information as possible from limited training data.

Another group of works use large-scale datasets of synthetic data for training. 3D-CODED [23] is an encoder-decoder architecture that predicts the correspondence by learning a surface parameterization and attempts to estimate the deformation from the template shape to the test one. Transmatch [72] is a transformer-based model that uses an attention mechanism to learn the underlying structure of the geometry. Other works utilizing large amounts of data [10, 31, 76] mainly focus on point cloud registration, and a group of works learn the shape deformation using data-efficient architectures [20, 70].

We combine the advantages of both categories of models by training a large-scale method based on functional maps that leverages the power of denoising diffusion models.

Denoising Diffusion Models. Diffusion models have become popular in many areas of visual computing; see the recent survey for details [53]. Several diffusion-based generative models have been proposed [66, 67], and the simplified learning process of denoising diffusion probabilistic models (DDPMs) enabled the image synthesis at unprecedented quality [25]. Various conditioning mechanisms such as class labels, textual descriptions, or segmentation maps have been used to guide the diffusion process [59]. While diffusion models quickly found applications in areas beyond imaging such as video [26, 27] and 3D content generation [36, 54], their application to shape correspondence estimation has been limited so far to extracting descriptors

from images of meshes [17] or segmentation maps [1] generated by foundational models. Our work is the first to use DDPMs to directly predict the functional maps between pairs of shapes to obtain the correspondences.

Sign Ambiguity of Laplacian Eigenvectors. Since for any eigenvector ϕ_i , its negative version $-\phi_i$ is also an eigenvector, the Laplace-Beltrami eigenbasis suffers from sign ambiguity. Additionally, eigenvalues can have higher multiplicity and make the intrinsic ordering non-unique. This symmetry needs to be taken into account when processing the eigenvectors [8, 48, 63].

In graph learning, Laplacian eigenvectors are used to encode information about the structure of a graph [6, 32], and several methods were proposed to address the sign ambiguity. Laplacian Canonization [38] proposes to find the coordinate axis on which the projection of the eigenvector has the largest angle and fixes the projection to be positive. SAN [30] obtains sign-invariant operators using absolute subtraction and product between a pair of nodes, this only considers the relative sign between queries. SignNet [34] learns a sign-invariant embedding and Dwivedi et al. [18] learns on all possible sign combinations.

The methods described above are designed for graphs with a small number of vertices. For point clouds, Linearly Invariant Embedding [41] considered the problem of learning the basis functions directly from the input data. However, the majority of works on 3D shapes employ the sign-equivariant approach, where a sign-dependent functional map is computed from descriptor functions in a pre-computed Laplace-Beltrami eigenbasis. In our work, we propose to address the sign ambiguity problem using a learning-based method that assigns a specific combination of signs to the eigenvectors of any human shape, which is learned directly from the data in an unsupervised way.

3. Background

Notation. Given a shape S represented as a triangular mesh with v vertices, we compute its Laplace matrix L [45] and the first n eigenvectors of L corresponding to the eigenvalues $\lambda_1 \leq \dots \leq \lambda_n$. A is then the diagonal vertex-area matrix associated with L , computed by assigning one-third of the total area of all faces incident to the corresponding vertex.

We denote matrices of n functions on the vertices of S by uppercase letters: $\Phi \in \mathbb{R}^{v \times n}$ for the matrix of eigenvectors, $\Sigma \in \mathbb{R}^{v \times n}$ for the matrix of learned features. The individual eigenvectors and feature vectors are denoted by lowercase letters: $\phi_i \in \mathbb{R}^v$ for the i -th eigenvector, $\varsigma_i \in \mathbb{R}^v$ for the i -th feature vector. Finally, $\sigma \in \{-1, 1\}^n$ represents a vector consisting of n signs.

3.1. Functional Maps

Our method is built upon the framework of functional maps [49, 50]. Consider the point-wise map $\Pi_{21} \in \{0, 1\}^{v_2 \times v_1}$ between two meshes S_1 and S_2 . The point-wise map is a permutation matrix, and due to its large size, it cannot be processed efficiently. The functional map $C_{12} \in \mathbb{R}^{n \times n}$ is the spectral representation of Π_{21} , which is computed as

$$C_{12} = \Phi_2^\dagger \Pi_{21} \Phi_1, \quad (1)$$

where “ \dagger ” denotes the pseudo-inverse. The functional map efficiently encodes the point-wise map in a low-dimensional representation, since $n \ll v_1, v_2$.

In a standard pipeline, learned or handcrafted p -dimensional descriptor functions are computed on each shape, $F_1 \in \mathbb{R}^{v_1 \times p}$, $F_2 \in \mathbb{R}^{v_2 \times p}$. The functional map is then obtained by solving the linear system [50]:

$$C_{12} = \arg \min_C \left\| C \Phi_1^\dagger F_1 - \Phi_2^\dagger F_2 \right\|_2^2, \quad (2)$$

which is usually further regularized [15, 47]. The point-wise map can be recovered from the functional map and the eigenvectors using nearest neighbor search [49, 51].

3.2. Sign Ambiguity

The functional map is defined in a basis spanned by the eigenvectors of the Laplacian on each shape, as can be seen from Eq. (1). However, this basis is not unique since for each eigenvector ϕ_i , $-\phi_i$ is also a valid eigenvector corresponding to the same eigenvalue λ_i . Due to sign ambiguity, there are 2^n possible basis combinations on each shape.

The eigenvectors returned by a numerical eigensolver will have a random sign combination, and mathematically it is impossible to select some specific sign of eigenvectors. However, several works demonstrate that the choice of the sign can be determined by the underlying data using the projection operator [8, 34, 38]. An intuitive example arises in the principal component analysis: Each eigenvector should point in the same direction as the points it is representing. This can be achieved by projecting the singular vector onto the data vectors and changing its sign to make the projection positive. This approach allows to select a canonical direction for the first few eigenvectors.

Sign ambiguity is a special case of basis ambiguity when all eigenvalues are distinct. The more general basis ambiguity occurs if an eigenvalue λ_i has multiplicity degree $d_i > 1$. Then any d_i vectors forming an orthogonal basis in the subspace spanned by its eigenvectors ($\phi_{i+1}, \phi_{i+2} \dots \phi_{i+d_i}$) are also valid eigenvectors. Although the basis ambiguity is difficult to deal with, in practice high multiplicities do not occur often and are less common in low-order eigenvectors [29, 50].

3.3. Denoising Diffusion Models

Given a dataset of examples drawn independently from a data distribution $q(x)$, diffusion models aim to learn the underlying data distribution by sequentially denoising random noise samples [25, 53, 66].

The forward diffusion process takes a real data point x_0 and incrementally adds to it a small amount of Gaussian noise, producing a sequence of T noisy samples x_1, \dots, x_T . The step sizes are controlled by a variance schedule $\{\beta_t \in (0, 1)\}_{t=1}^T$. With the larger steps t , the noisy sample x_t further deviates from the original sample. At $T \rightarrow \infty$, it is close to the Gaussian distribution, $x_T \sim N(x_T; 0, I)$. The reverse process recreates the original sample by iteratively removing noise from an input x_T drawn from the Gaussian distribution. Assuming that the reverse conditional probability is conditioned on x_0 , $q(x_{t-1} | x_t, x_0) = N(x_{t-1}; \tilde{\mu}(x_t, x_0), \tilde{\beta}_t I)$, we can obtain $\tilde{\mu}_t = \frac{1}{\sqrt{\alpha_t}} \left(x_t - \frac{1-\alpha_t}{\sqrt{1-\alpha_t}} \epsilon_t \right)$, where $\alpha_t = 1 - \beta_t$ and $\bar{\alpha}_t = \prod_{i=1}^t \alpha_i$.

Instead of directly predicting the denoised sample $\tilde{\mu}_t$ with a neural network, we can predict the noise content $\epsilon_\theta(x_t, t)$ from the input x_t at time step t [25]. Such a model is trained with a denoising score-matching objective: $\mathcal{L} = E_{t \sim [1, T], x_0, \epsilon_t} \left[\|\epsilon_t - \epsilon_\theta(x_t, t)\|_2^2 \right]$.

4. Denoising Functional Maps

This section introduces Denoising Functional Maps (DenoisFM), our approach for shape correspondence estimation; see Fig. 2 for the method overview. Since functional maps are square low-dimensional matrices (see Sec. 3.1), we use a standard neural architecture based on a 2D U-Net [61] as a backbone. We aim to train our model on a large collection of shapes with diverse geometry. Since functional maps are defined for shape pairs, for a dataset with m shapes the model would have to learn m^2 functional maps. Instead of this naive approach, we consider the correspondences to a single template shape, following previous works [23, 72]. As a result, the training data includes only m functional maps, one for each shape in the dataset.

A functional map is defined in a specific basis of Laplacian eigenvectors, and knowing the exact basis combination is necessary to convert it to a point-wise correspondence map. Therefore, we compute the basis first and then condition the diffusion model on it; the model then returns the corresponding functional map. To reduce the complexity of the problem caused by the sign ambiguity of basis eigenvectors, we utilize a sign correction network to select a specific combination of signs for the basis.

DenoisFM consists of two components: the DDPM for functional map prediction (Sec. 4.1) with post-processing that filters out low-quality solutions using Dirichlet energy

of the point-wise map (Sec. 4.1.2), and the sign corrector for the Laplacian eigenvectors (Sec. 4.2).

4.1. Denoising Diffusion Component

4.1.1. Overview

We next describe the training and inference of the diffusion component of DenoisFM. For training, we use a large collection of shapes and a template. For each shape S in the dataset, we compute an eigenbasis Φ , a template-wise functional map C_{1T} , and conditioning $y = y(S, \Phi)$ which incorporates geometric details of the input shape and information about the basis. The exact form of conditioning will be specified in Sec. 4.3. We use the training objective of denoising diffusion probabilistic models (DDPMs) [25]:

$$\mathcal{L}_{\text{DDPM}} = E_{x, \epsilon \sim N(0, 1), t} \left[\|\epsilon - \epsilon_\theta(x_t, t, y)\|_2^2 \right], \quad (3)$$

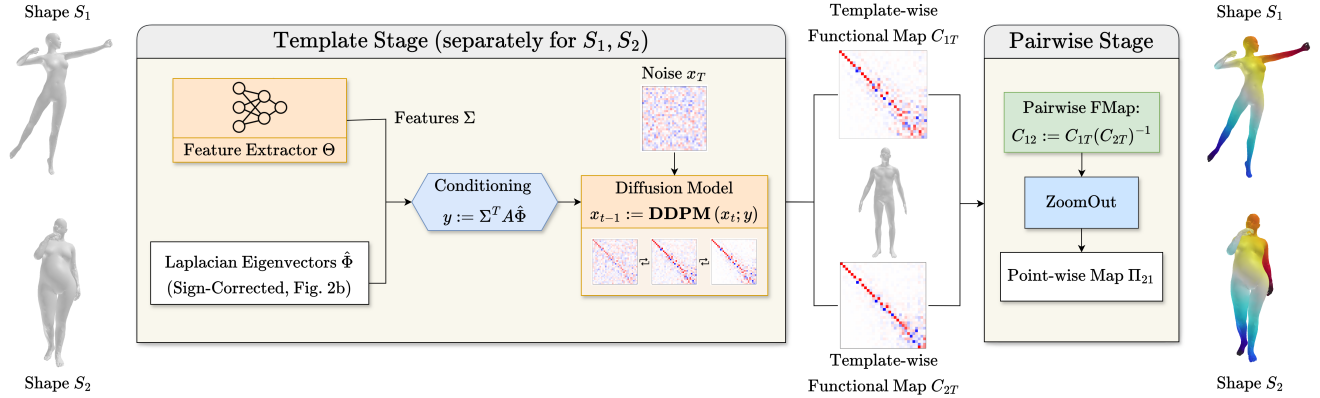
where ϵ_θ is the amount of noise predicted by a 2D UNet [60], x_t is a noisy version of the input $x_0 := C_{1T}$, and t is the time step uniformly sampled from $\{1, \dots, T\}$.

The inference pipeline consists of two stages, see Fig. 2a. In the template stage, for each individual shape in the evaluation dataset, we obtain an eigenbasis, calculate the conditioning, and predict the template-wise functional map using the diffusion model. Note that the inference of DDPMs is time-consuming due to the large number of denoising steps and can take several hours for high-dimensional functional maps. Because the predicted maps refer to the template, we need to run the denoising process only once for each shape.

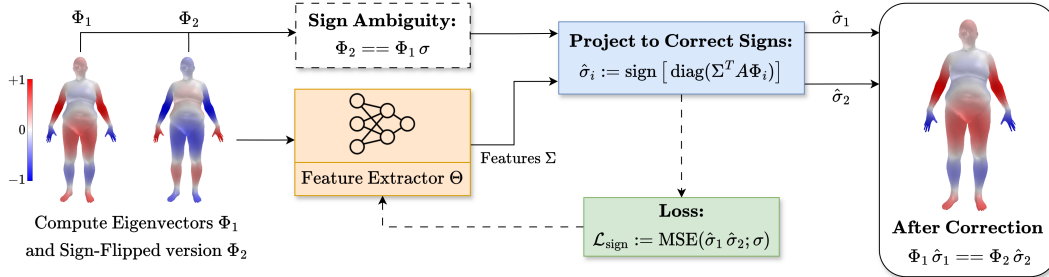
In the pairwise stage, for each test pair, we convert the respective template-wise functional maps into pairwise ones using the composition property [49]: $C_{12} = C_{1T}(C_{2T})^{-1}$. We then apply the Zoomout refinement [44] to increase the resolution of the functional maps. This spectral upsampling step has been shown to improve their accuracy, and our framework benefits from it without additional modifications. Finally, the functional map is converted into a point-wise map Π_{21} using nearest neighbor search.

4.1.2. Post-Processing of the Samples

Diffusion models are inherently probabilistic and their outputs may differ given the same conditioning but different initial noise [25]. To address this, we repeat the denoising process multiple times and filter out the low-quality results. The selection is based on the Dirichlet energy of the point-wise map [21, 40]: an accurate map should be smooth, with neighboring vertices on one shape matching neighboring vertices on the other. Therefore, we repeat both the template step and the pairwise step to produce multiple point-wise maps. We can then either report the map with the lowest Dirichlet energy or combine the results of several smoothest maps. To do this, for each query point on the source mesh, we gather potential matching points on the target mesh and



(a) **Functional map prediction using a diffusion model.** For each unique shape in the dataset, we obtain surface features using a feature extractor, as well as a sign-corrected eigenbasis (Sec. 4.2). Both are used for conditional prediction of the template-wise functional map using a diffusion model, performed separately for each shape. The pairwise functional maps are obtained through the map composition property, upsampled using ZoomOut [44], and converted to pointwise maps.



(b) **Learned sign correction.** The eigenvectors returned by a numerical eigensolver have random signs. To select a specific sign, we project the eigenvectors onto the learned correction vector obtained with a feature extractor, and make the projection positive. The sign correction network is trained in an unsupervised manner: learning to correct eigenvectors that have random signs.

Figure 2. **Overview of DenoisFM.** (a) A pair of shapes is matched using a DDPM model. (b) The signs of eigenvectors are corrected through a learned projection vector.

select the one with the smallest total distance to the other candidates (see Supplement B.3). We found the map selection step to be very important in determining the final accuracy of the method.

4.2. Learned Sign Correction

4.2.1. Intuition

The diffusion model should be conditioned on the basis eigenvectors and predict the functional map for that particular basis. Theoretically, the model could be trained using random basis combinations, as was done in Dwivedi *et al.* [18] for graph networks. However, this would dramatically increase the amount of training data.

Hence, we follow a more effective approach: we select a specific basis by fixing the sign of the Laplacian eigenvectors on each shape. Previous works infer the sign from the underlying data using the projection operator (see Sec. 3.2). Therefore, suppose that $\Sigma \in \mathbb{R}^{v \times n}$ is a set of per-vertex features inferred from the mesh geometry, one for each eigenvector. The sign of the eigenvectors can be selected by pro-

jecting the features Σ onto the eigenvectors Φ and making the corresponding projections positive. This can be written as:

$$\begin{aligned} \hat{\sigma} &:= \text{sign} [\text{diag}(\Sigma^T A \Phi)], \\ \hat{\Phi} &:= \Phi \hat{\sigma}, \end{aligned} \quad (4)$$

where “diag(\cdot)” and “sign(\cdot)” denote matrix diagonal and sign extraction operators, A is the diagonal vertex-area matrix. To illustrate this, suppose we are given a human mesh and a single feature vector c_i , which is a binary vector with ones for points on the left hand, and zeros otherwise. After performing the procedure described in Eq. (4), the corrected eigenvector $\hat{\phi}_i$ will be predominantly positive on the left hand.

4.2.2. Training the Sign Corrector

In practice, the signs of eigenvectors should be selected using priors learned by a neural network. We define the **learned correction vector** $\Sigma := \Theta(S)$, where Θ is a trainable per-vertex feature extractor. If we perform the eigen-decomposition with a numerical solver twice on the same

mesh and get two sets of eigenvectors Φ_1 and Φ_2 , due to the sign ambiguity, the difference between them can be written as $\Phi_2 = \Phi_1 \sigma$, where $\sigma \in \{-1, 1\}^n$ is the ground-truth sign difference. Now we perform the sign correction using Eq. (4), after which we expect the corrected eigenvectors to be equal to each other:

$$\begin{aligned}\hat{\Phi}_1 &= \hat{\Phi}_2, \\ \Phi_1 \hat{\sigma}_1 &= \Phi_2 \hat{\sigma}_2,\end{aligned}\tag{5}$$

where $\hat{\sigma}_1, \hat{\sigma}_2 \in \{-1, 1\}^n$ are the predicted combinations of correction signs. After substitution and using $\hat{\sigma}_1 \hat{\sigma}_1 = I$, we obtain:

$$\begin{aligned}\Phi_1 \hat{\sigma}_1 &= \Phi_1 \sigma \hat{\sigma}_2, \\ \hat{\sigma}_1 &= \sigma \hat{\sigma}_2, \\ \hat{\sigma}_1 \hat{\sigma}_2 &= \sigma.\end{aligned}\tag{6}$$

As a result, the difference between the predicted correction signs should be the same as the ground-truth sign difference, and we can use this as our unsupervised training objective with a mean square error function:

$$\mathcal{L}_{\text{sign}} = \text{MSE}(\hat{\sigma}_1 \hat{\sigma}_2; \sigma)\tag{7}$$

Note that the sign operator in Eq. (4) is not differentiable. Therefore, during training, we set $\hat{\sigma}_1$ and $\hat{\sigma}_2$ to be the diagonal elements of the projections, rather than their signs, assuming that the correction vectors and eigenvectors have unit norm. The training objective of the feature extractor (Eq. (7)) then forces the elements of $\hat{\sigma}_1$ and $\hat{\sigma}_2$ to be as close to -1 or 1 as possible. The absolute value can be interpreted as confidence in the predicted sign: values close to ± 1 mean high confidence.

In practice, we found that a network trained this way converges quite quickly on a dataset of human meshes. Our method returns the same corrected eigenbasis 95–99% of the time for the first hundred Laplacian eigenvectors. The accuracy of the sign correction and its impact on the distribution of functional maps are discussed in Supplement A.

4.3. Choice of Conditioning

Conditioning of the diffusion model should include two parts: the basis information and the geometric features of the shape. The former can be provided simply via the sign-corrected eigenvectors $\hat{\Phi}$. They additionally represent the spectral embedding of the shape and convey the full intrinsic information. As for the latter, during the training of the sign-correction network, the useful features will be encoded in the learned correction vector Σ . Therefore, we propose to project the learned correction vectors onto the sign-corrected eigenvectors:

$$\text{Conditioning } y = \Sigma^T A \hat{\Phi}.\tag{8}$$

This form of conditioning has two important properties. First, it has the same dimensions as the functional map.

Therefore, we can condition the diffusion model using a simple concatenation, where the conditioning matrix is concatenated with the intermediate denoising targets and passed through the score estimator as input [25, 75]. Second, it is independent of the number of vertices, making it scalable to large meshes.

5. Training and Experimental Results

This section describes the steps for generating the training data for our model (Sec. 5.1) as well as the experimental results on several challenging datasets (Secs. 5.2–5.5). The evaluation of the sign correction network, additional comparison, and the ablation studies can be found in Supplement A and C. Since our model is designed to be trained on large and diverse shape collections, it can be applied to multiple (reminiscent) shape classes without re-training. This reduces the need for small category-specific training sets. We focus on datasets with human-like shapes as their combined volume allows versatile training and comparison of our new DDPM-based approach with the previous state of the art.

5.1. Training Data and Implementation

Our model consists of two independent components: a denoising diffusion model that predicts the functional map and a sign correction network based on a per-vertex feature extractor. To reduce computational overhead, we train them separately on the respective datasets.

5.1.1. Denoising Diffusion

Diffusion models require large amounts of training data with hundreds of thousands of examples. Therefore, we follow 3D-CODED [23] and use the SURREAL [73] dataset with 230,000 human meshes generated with SMPL [37]. All its meshes are smooth and have the same vertex structure. To make the connectivity more diverse, we remesh each mesh [28, 46] and randomly simplify the number of faces using Quadric Edge Collapse [22]. In 65% of the cases, we simplify the entire mesh resulting in uniform connectivity. In the remaining 35% of the cases, we simplify only a small subset of the mesh to add non-even connectivity to the training data. After remeshing, we correct the signs of the eigenvectors using a pre-trained sign correction network (Sec. 4.2) and compute the functional map to the template shape. We only store the functional maps and conditioning matrices to save memory requirements. The data generation takes 10 hours using parallel processing.

We use the standard DDPM [25] implemented in Diffusers [74] and distributed training with Accelerate [24]. We train models that predict 32, 64, and 96-dimensional functional maps for 100 epochs on eight A40 GPUs, which takes 1, 8, and 30 hours respectively. The inference at the

template stage takes 1, 7, and 27 minutes for each shape in the dataset. The pairwise stage takes 30 seconds per pair.

5.1.2. Sign Correction Network

The per-vertex feature extractor of the sign correction network is based on DiffusionNet [65] (not to be confused with denoising diffusion) with six blocks and 128 WKS descriptors [5] as input. This architecture was designed for small shape matching datasets, so we used 1000 randomly selected meshes from SURREAL for training. Each of them was randomly remeshed and simplified without adding anisotropy. The sign correction network is trained for $5 \cdot 10^4$ iterations, which takes one hour on a single A40 GPU; the inference takes a few seconds per shape.

5.2. Near-Isometric Shape Matching

Datasets. We evaluate our method on three widely used datasets: FAUST [7], SCAPE [3] and SHREC’19 [43]. Following previous works, we use their more challenging remeshed versions [15, 56]:

- The **FAUST** dataset contains meshes of 10 humans with various body types in 10 poses, 100 in total. The training/testing split is 80/20.
- The **SCAPE** dataset includes 71 meshes of the same person in different poses, the last 20 are used for testing.
- The **SHREC’19** dataset is composed of 44 shapes with diverse body types and poses, arguably the most challenging of the three. This dataset does not have a train split and is used for testing only. Following [11], we removed shape 40 since it is the only partial non-closed shape.

Baselines. We compare our approach with two categories of non-rigid shape correspondence methods. The first includes large-scale template-based models trained on SURREAL: 3D-CODED [23] and TransMatch [72], i.e., our main competitors as our work belongs to the same group. The second category includes descriptor-based models: ULRSSM [11], DiffZO [39], ConsistentFMaps [69], GeomFMaps [15], AttentiveFMaps [33], DUO-FMNet [16], SSL [10], SmS [12]. Since our and other methods can be applied to any shape class, we do not include template fitting methods such as NICP [42], which typically focus on human scans and incorporate explicit human body priors.

To compare both categories of baselines fairly, we note that SCAPE is too small to train large models. On the other hand, FAUST was created with SMPL [37] like SURREAL, and includes a sufficient diversity of body types and poses. Therefore, we follow [10, 11, 69] and train large models on SURREAL, descriptor-based models on FAUST, and evaluate them on three test datasets. A comparison with the baselines trained on both FAUST and SCAPE can be found in Supplement C.3.

Model	Category	F.r	S.r	S’19_r
3D-CODED	Large-Scale	2.5	16.1	17.3
TransMatch		1.7	15.3	21.0
DUO-FMNet	Descriptor-Based	2.5	4.2	6.4
GeomFMaps		1.9	2.4	7.9
AttentiveFMaps		1.9	2.6	5.8
ConsistentFMaps		2.3	2.6	3.8
SSL		2.0	3.1	4.0
DiffZO		1.9	2.4	4.2
ULRSSM		1.6	2.2	5.7
SmS		1.4	3.3	6.2
Ours – 64×64	1.8	2.3	3.5	
Ours – 96×96	1.7	2.1	3.6	

Table 1. Mean geodesic errors ($\times 100$) on the remeshed FAUST, SCAPE, and SHREC’19 datasets. The **best** results are highlighted. Large-scale methods are trained on SURREAL, and descriptor-based methods on FAUST. Here and in the following, the results of our model are averaged across 5 runs.

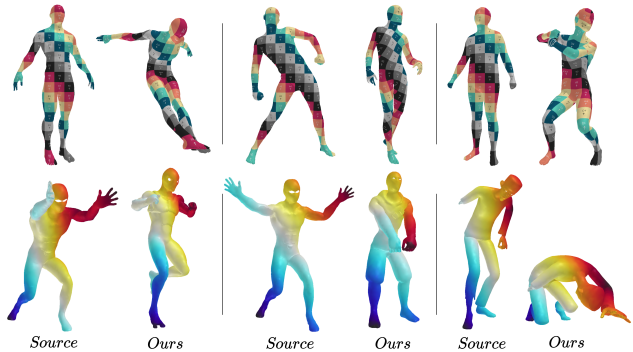


Figure 3. Qualitative results by our approach on SHREC’19 (top) and DT4D (bottom) datasets; see also Supplement C.2.

Results. We report the mean geodesic error of our model and the baselines in Table 1. Compared to other large-scale methods trained on SURREAL, our work generalizes well to meshes from SCAPE and SHREC’19. A common problem in large-scale baselines is predicted point maps with incorrect symmetry. This is caused by the fact that the geometry of the evaluation meshes has fewer fine-scale details such as fingers, which help to disambiguate the internal symmetry. Our work avoids overfitting to fine-scale details of SURREAL by using data augmentation (Sec. 5.1). As a result, we can utilize large amounts of data more effectively than previous works.

Compared to descriptor-based methods, our results are on par on all datasets (especially SHREC’19), demonstrating our excellent performance on diverse shape classes. We can see that most descriptor-based methods can generalize to non-SMPL meshes, but none of them show competitive performance on all three datasets simultaneously.

We show the qualitative results of our model on several

Model	Category	F _a	S _a
3D-CODED	Large	2.9	16.9
TransMatch	Scale	2.7	16.2
DUO-FMNet		3.0	4.4
GeomFMaps	Descriptor Based	3.2	3.8
AttentiveFMaps		2.4	2.8
ConsistentFMaps		2.6	2.7
ULRSSM		1.9	2.4
Ours - 64×64		2.1	2.3
Ours - 96×96		2.0	2.2

Table 2. Results on the anisotropic versions of FAUST and SCAPE. Large-scale methods are trained on SURREAL, and descriptor-based methods on FAUST.

challenging meshes from SHREC’19 in Fig. 3. Even though these shapes include high-frequency details such as muscles, in contrast to the smooth shapes typically generated by SMPL, our model is able to obtain correct correspondences.

5.3. Matching with Anisotropic Meshing

Datasets. To evaluate the robustness of our method to different connectivity, we use the anisotropically remeshed versions of FAUST and SCAPE [16], denoted F_a and S_a, respectively. In these datasets, the triangle scale is uneven, ranging from small and densely packed triangles on one side of the mesh to large and coarse triangulation on the other. As a result, models that are sensitive to mesh connectivity will likely fail to predict the correct maps.

Results. Table 2 shows the matching results. Both large-scale and descriptor-based methods experience performance drops on anisotropically remeshed datasets. In contrast, our method is more robust to changes in mesh connectivity. We attribute this to our design choices, such as diversifying the vertex structure of the training data and using conditioning that is independent of the number of vertices.

5.4. Zero-Shot Shape Matching

Datasets. Generalization to shape types not observed during training is a desirable property in many shape matching applications. To evaluate our model on unseen data, we use the non-isometric DT4D dataset [40] that consists of nine humanoid shape classes. While typically, 198 shapes are defined for training and 95 for testing, we instead make the evaluation more challenging by training on human datasets, SURREAL or FAUST. This can be viewed as a zero-shot setting, since most of the test shapes are different from the training data (see Supplement C.2 for an illustration).

Results. Our proposed experimental setup is challenging due to the differences between the training and evaluation

Class	Intra			Inter		
	Ours	[11]	[69]	Ours	[11]	[69]
manneq.	1.0	1.0	1.6	3.3	4.0	4.5
zlorp	1.1	1.3	2.1	4.2	6.9	4.2
crypto	1.1	1.5	2.4	–	–	–
prisoner	1.1	1.1	2.1	29.6	20.5	26.7
ninja	1.4	5.6	2.2	4.3	16.2	7.1
ortiz	9.3	4.4	2.5	–	–	–
mousey	10.2	2.7	5.2	–	–	–
drake	10.6	1.0	2.1	10.4	8.2	4.5
skeletonz.	16.3	1.4	1.4	49.4	36.5	48.0

Table 3. Results on shape classes from DT4D [40]. The best results are highlighted, where applicable. Classes *mousey* and *ortiz* are not present in inter-class split. All inter-class evaluation pairs have the format “*crypto* vs other class”, so *crypto* is also excluded.

shapes. Therefore, we use a lower-resolution model predicting a 32×32 functional map, results of all our models are shown in Supplement C.6. We compare our method with recent unsupervised descriptor-based approaches: ConsistentFMaps [69] and ULRSSM [11].

The mean geodesic errors per class for inter- and intra-category splits are shown in Table 3, additional comparison can be found in Supplement C.8. Our method achieves accurate matching for most shape classes in both splits, demonstrating the ability of our method to generalize to data unseen during training. We show the qualitative examples in Fig. 3.

5.5. Application to Animal Shapes

Datasets. To show the generality of our method to shape classes other than humans, we test our approach on the SMAL dataset containing seven animal types. We take the 32/17 split from [16], where all categories are present in train/test sets. While the original training set is sufficient for descriptor-based baselines, it is too small for our model. To address this, we use the fitted parameters of the SMAL parametric model [77] and randomly vary the pose of each training animal, generating a total of 64,000 meshes. We use the mean SMAL shape as a template. Note that this generated dataset conveys little new information, since e.g., there are only three different types of lions.

Results. Table 4 shows the results of our 64×64 model. Although the training data for our method lacks sufficient diversity, we achieve comparable performance to the baselines. Therefore, given enough training data, we believe our method can be applied to any shape class.

6. Conclusion

We presented DenoisFM, an approach of a new class for shape correspondence estimation. Our model is trained on

Class	Ours	[11]	[69]
wolf	3.4	3.4	4.4
dog	3.5	3.5	4.5
horse	3.7	3.8	4.4
cow	3.8	3.8	4.4
lion	4.0	3.8	4.9
fox	4.7	3.6	4.9
hippo	7.6	9.9	7.9
mean	4.3	4.3	4.8

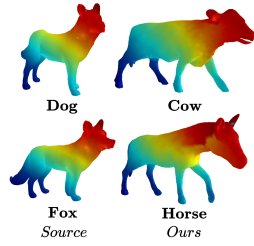


Table 4. Results on the SMAL dataset [16], all categories are present in train/test sets. We additionally show separate results for each category, e.g. lions vs. everything.

a large dataset of synthetic human meshes and predicts the functional map between a pair of shapes using a denoising diffusion model. DenoisFM achieves correspondence accuracy on par with state-of-the-art methods across multiple datasets. The key advantage of our work is its generalization ability to human and humanoid shapes that differ noticeably from the training data, as well as competitive performance on animal shapes. Therefore, DenoisFM bridges the gap between previous large-scale and descriptor-based approaches by efficiently leveraging large amounts of data, opening up a new direction for using diffusion models in shape correspondence estimation.

Acknowledgement. ZL acknowledges the support of the DFG Sachbeihilfe grant LA 5191/2-1.

References

- [1] Ahmed Abdelreheem, Abdelrahman Eldesokey, Maks Ovsjanikov, and Peter Wonka. Zero-shot 3d shape correspondence. In *SIGGRAPH Asia Conference Papers*, 2023. 2, 3
- [2] Hervé Abdi and Lynne J Williams. Principal component analysis. *Wiley interdisciplinary reviews: computational statistics*, 2(4):433–459, 2010. 12
- [3] Dragomir Anguelov, Praveen Srinivasan, Daphne Koller, Sebastian Thrun, Jim Rodgers, and James Davis. Scape: shape completion and animation of people. In *ACM SIGGRAPH 2005 Papers*, pages 408–416. 2005. 2, 7
- [4] Souhaib Attaiki, Gautam Pai, and Maks Ovsjanikov. Dpfm: Deep partial functional maps. In *2021 International Conference on 3D Vision (3DV)*, pages 175–185. IEEE, 2021. 1
- [5] Mathieu Aubry, Ulrich Schlickewei, and Daniel Cremers. The wave kernel signature: A quantum mechanical approach to shape analysis. In *International Conference on Computer Cision (ICCV) workshops*, 2011. 2, 7
- [6] Mikhail Belkin and Partha Niyogi. Laplacian eigenmaps for dimensionality reduction and data representation. *Neural computation*, 15(6):1373–1396, 2003. 3
- [7] Federica Bogo, Javier Romero, Matthew Loper, and Michael J Black. Faust: Dataset and evaluation for 3d mesh registration. In *Proceedings of the IEEE conference on computer vision and pattern recognition*, pages 3794–3801, 2014. 2, 7, 12
- [8] Rasmus Bro, Evrim Acar, and Tamara G Kolda. Resolving the sign ambiguity in the singular value decomposition. *Journal of Chemometrics: A Journal of the Chemometrics Society*, 22(2):135–140, 2008. 3
- [9] Michael M Bronstein and Iasonas Kokkinos. Scale-invariant heat kernel signatures for non-rigid shape recognition. In *2010 IEEE computer society conference on computer vision and pattern recognition*, pages 1704–1711. IEEE, 2010. 1, 2
- [10] Dongliang Cao and Florian Bernard. Self-supervised learning for multimodal non-rigid 3d shape matching. In *Proceedings of the IEEE/CVF Conference on Computer Vision and Pattern Recognition*, pages 17735–17744, 2023. 2, 7
- [11] Dongliang Cao, Paul Roetzer, and Florian Bernard. Unsupervised learning of robust spectral shape matching. *ACM Transactions on Graphics*, 42(4):132:1–132:15, 2023. 1, 2, 7, 8, 9, 14, 15, 17
- [12] Dongliang Cao, Marvin Eisenberger, Nafie El Amrani, Daniel Cremers, and Florian Bernard. Spectral meets spatial: Harmonising 3d shape matching and interpolation. In *Computer Vision and Pattern Recognition (CVPR)*, 2024. 7, 15
- [13] Etienne Corman, Maks Ovsjanikov, and Antonin Chambolle. Supervised descriptor learning for non-rigid shape matching. In *ECCV Workshops*, 2014. 1
- [14] Huong Quynh Dinh, Anthony Yezzi, and Greg Turk. Texture transfer during shape transformation. *ACM Transactions on Graphics (ToG)*, 24(2):289–310, 2005. 1
- [15] Nicolas Donati, Abhishek Sharma, and Maks Ovsjanikov. Deep geometric functional maps: Robust feature learning for shape correspondence. In *Computer Vision and Pattern Recognition*, 2020. 2, 3, 7
- [16] Nicolas Donati, Etienne Corman, and Maks Ovsjanikov. Deep orientation-aware functional maps: Tackling symmetry issues in shape matching. In *Computer Vision and Pattern Recognition*, 2022. 7, 8, 9
- [17] Niladri Shekhar Dutt, Sanjeev Muralikrishnan, and Niloy J. Mitra. Diffusion 3d features (diff3f): Decorating untextured shapes with distilled semantic features. In *Proceedings of the IEEE/CVF Conference on Computer Vision and Pattern Recognition (CVPR)*, pages 4494–4504, 2024. 2, 3
- [18] Vijay Prakash Dwivedi, Chaitanya K Joshi, Anh Tuan Luu, Thomas Laurent, Yoshua Bengio, and Xavier Bresson. Benchmarking graph neural networks. *Journal of Machine Learning Research*, 24(43):1–48, 2023. 3, 5
- [19] Marvin Eisenberger, Zorah Lahner, and Daniel Cremers. Smooth shells: Multi-scale shape registration with functional maps. In *Computer Vision and Pattern Recognition (CVPR)*, 2020. 1
- [20] Marvin Eisenberger, David Novotny, Gael Kerchenbaum, Patrick Labatut, Natalia Neverova, Daniel Cremers, and Andrea Vedaldi. Neuromorph: Unsupervised shape interpolation and correspondence in one go. In *Computer Vision and Pattern Recognition*, 2021. 2
- [21] Danielle Ezuz, Justin Solomon, and Mirela Ben-Chen. Reversible harmonic maps between discrete surfaces. *ACM Transactions on Graphics (ToG)*, 38(2):1–12, 2019. 4

- [22] Michael Garland and Paul S Heckbert. Surface simplification using quadric error metrics. In *Proceedings of the 24th annual conference on Computer graphics and interactive techniques*, pages 209–216, 1997. 6
- [23] Thibault Groueix, Matthew Fisher, Vladimir G Kim, Bryan C Russell, and Mathieu Aubry. 3d-coded: 3d correspondences by deep deformation. In *European Conference on Computer Vision (ECCV)*, 2018. 2, 4, 6, 7
- [24] Sylvain Gugger, Lysandre Debut, Thomas Wolf, Philipp Schmid, Zachary Mueller, Sourab Mangrulkar, Marc Sun, and Benjamin Bossan. Accelerate: Training and inference at scale made simple, efficient and adaptable. <https://github.com/huggingface/accelerate>, 2022. 6
- [25] Jonathan Ho, Ajay Jain, and Pieter Abbeel. Denoising diffusion probabilistic models. *Advances in neural information processing systems*, 33:6840–6851, 2020. 1, 2, 4, 6
- [26] Jonathan Ho, William Chan, Chitwan Saharia, Jay Whang, Ruiqi Gao, Alexey Gritsenko, Diederik P Kingma, Ben Poole, Mohammad Norouzi, David J Fleet, et al. Imagen video: High definition video generation with diffusion models. *arXiv preprint arXiv:2210.02303*, 2022. 2
- [27] Jonathan Ho, Tim Salimans, Alexey Gritsenko, William Chan, Mohammad Norouzi, and David J Fleet. Video diffusion models. *Advances in Neural Information Processing Systems*, 35:8633–8646, 2022. 2
- [28] Hugues Hoppe, Tony DeRose, Tom Duchamp, John McDonald, and Werner Stuetzle. Mesh optimization. In *Proceedings of the 20th annual conference on Computer graphics and interactive techniques*, pages 19–26, 1993. 6
- [29] Tosio Kato. *Perturbation theory for linear operators*. Springer Science & Business Media, 2013. 3
- [30] Devin Kreuzer, Dominique Beaini, Will Hamilton, Vincent Létourneau, and Prudencio Tossou. Rethinking graph transformers with spectral attention. *Advances in Neural Information Processing Systems*, 34:21618–21629, 2021. 3
- [31] Itai Lang, Dvir Ginzburg, Shai Avidan, and Dan Raviv. Dpc: Unsupervised deep point correspondence via cross and self construction. In *2021 International Conference on 3D Vision (3DV)*, pages 1442–1451. IEEE, 2021. 2
- [32] Bruno Lévy. Laplace-beltrami eigenfunctions towards an algorithm that “understands” geometry. In *IEEE International Conference on Shape Modeling and Applications 2006 (SMI’06)*, pages 13–13. IEEE, 2006. 3
- [33] Lei Li, Nicolas Donati, and Maks Ovsjanikov. Learning multi-resolution functional maps with spectral attention for robust shape matching. *Advances in Neural Information Processing Systems*, 35:29336–29349, 2022. 7, 15
- [34] Derek Lim, Joshua Robinson, Lingxiao Zhao, Tess Smidt, Suvrit Sra, Haggai Maron, and Stefanie Jegelka. Sign and basis invariant networks for spectral graph representation learning. *arXiv preprint arXiv:2202.13013*, 2022. 3
- [35] Or Litany, Tal Remez, Emanuele Rodola, Alex Bronstein, and Michael Bronstein. Deep functional maps: Structured prediction for dense shape correspondence. In *International Conference on Computer Vision (ICCV)*, 2017. 2
- [36] Zhen Liu, Yao Feng, Michael J Black, Derek Nowrouzezahrai, Liam Paull, and Weiyang Liu. Meshdiffusion: Score-based generative 3d mesh modeling. *arXiv preprint arXiv:2303.08133*, 2023. 2
- [37] Matthew Loper, Naureen Mahmood, Javier Romero, Gerard Pons-Moll, and Michael J. Black. SMPL: A skinned multi-person linear model. *ACM Trans. Graphics (Proc. SIGGRAPH Asia)*, 34(6):248:1–248:16, 2015. 1, 2, 6, 7
- [38] George Ma, Yifei Wang, and Yisen Wang. Laplacian canonization: A minimalist approach to sign and basis invariant spectral embedding. *Advances in Neural Information Processing Systems*, 36, 2024. 3
- [39] Robin Magnet and Maks Ovsjanikov. Memory-scalable and simplified functional map learning. In *Proceedings of the IEEE/CVF Conference on Computer Vision and Pattern Recognition*, pages 4041–4050, 2024. 7
- [40] Robin Magnet, Jing Ren, Olga Sorkine-Hornung, and Maks Ovsjanikov. Smooth non-rigid shape matching via effective dirichlet energy optimization. In *3D Vision (3DV)*, 2022. 2, 4, 8, 17
- [41] Riccardo Marin, Marie-Julie Rakotosaona, Simone Melzi, and Maks Ovsjanikov. Correspondence learning via linearly-invariant embedding. *Advances in Neural Information Processing Systems*, 33:1608–1620, 2020. 3
- [42] Riccardo Marin, Enric Corona, and Gerard Pons-Moll. Nicp: neural icp for 3d human registration at scale. In *European Conference on Computer Vision*, 2024. 1, 7
- [43] Simone Melzi, Riccardo Marin, Emanuele Rodolà, Umberto Castellani, Jing Ren, Adrien Poulenard, Peter Wonka, and Maks Ovsjanikov. Shrec 2019: Matching humans with different connectivity. In *Eurographics Workshop on 3D Object Retrieval*, page 3. The Eurographics Association, 2019. 2, 7
- [44] Simone Melzi, Jing Ren, Emanuele Rodola, Abhishek Sharma, Peter Wonka, and Maks Ovsjanikov. Zoomout: Spectral upsampling for efficient shape correspondence. *arXiv preprint arXiv:1904.07865*, 2019. 1, 4, 5, 16, 17
- [45] Mark Meyer, Mathieu Desbrun, Peter Schröder, and Alan H Barr. Discrete differential-geometry operators for triangulated 2-manifolds. In *Visualization and mathematics III*, pages 35–57. Springer, 2003. 3
- [46] Alessandro Muntoni and Paolo Cignoni. PyMeshLab, 2021. 6
- [47] Dorian Nogneng and Maks Ovsjanikov. Informative descriptor preservation via commutativity for shape matching. In *Computer Graphics Forum*, pages 259–267. Wiley Online Library, 2017. 3
- [48] Maks Ovsjanikov, Jian Sun, and Leonidas Guibas. Global intrinsic symmetries of shapes. In *Computer graphics forum*, pages 1341–1348. Wiley Online Library, 2008. 3
- [49] Maks Ovsjanikov, Mirela Ben-Chen, Justin Solomon, Adrian Butscher, and Leonidas Guibas. Functional maps: a flexible representation of maps between shapes. *ACM Transactions on Graphics (ToG)*, 31(4):1–11, 2012. 1, 2, 3, 4
- [50] Maks Ovsjanikov, Etienne Corman, Michael Bronstein, Emanuele Rodolà, Mirela Ben-Chen, Leonidas Guibas, Frederic Chazal, and Alex Bronstein. Computing and processing correspondences with functional maps. In *SIGGRAPH ASIA 2016 Courses*, pages 1–60. 2016. 2, 3

- [51] Gautam Pai, Jing Ren, Simone Melzi, Peter Wonka, and Maks Ovsjanikov. Fast sinkhorn filters: Using matrix scaling for non-rigid shape correspondence with functional maps. In *Computer Vision and Pattern Recognition*, 2021. 3
- [52] Ulrich Pinkall and Konrad Polthier. Computing discrete minimal surfaces and their conjugates. *Experimental mathematics*, 2(1):15–36, 1993. 2
- [53] Ryan Po, Wang Yifan, Vladislav Golyanik, Kfir Aberman, Jonathan T Barron, Amit Bermano, Eric Chan, Tali Dekel, Aleksander Holynski, Angjoo Kanazawa, et al. State of the art on diffusion models for visual computing. In *Computer Graphics Forum*, 2024. 2, 4
- [54] Ben Poole, Ajay Jain, Jonathan T Barron, and Ben Mildenhall. Dreamfusion: Text-to-3d using 2d diffusion. *arXiv preprint arXiv:2209.14988*, 2022. 2
- [55] Neng Qian, Jiayi Wang, Franziska Mueller, Florian Bernard, Vladislav Golyanik, and Christian Theobalt. HTML: A Parametric Hand Texture Model for 3D Hand Reconstruction and Personalization. In *European Conference on Computer Vision (ECCV)*, 2020. 1
- [56] Jing Ren, Adrien Poulenard, Peter Wonka, and Maks Ovsjanikov. Continuous and orientation-preserving correspondences via functional maps. *ACM Transactions on Graphics (TOG)*, 37(6):1–16, 2018. 7
- [57] Jing Ren, Simone Melzi, Peter Wonka, and Maks Ovsjanikov. Discrete optimization for shape matching. In *Computer Graphics Forum*, pages 81–96. Wiley Online Library, 2021. 1
- [58] Emanuele Rodolà, Luca Cosmo, Michael M Bronstein, Andrea Torsello, and Daniel Cremers. Partial functional correspondence. In *Computer graphics forum*, pages 222–236. Wiley Online Library, 2017. 1
- [59] Robin Rombach, Andreas Blattmann, Dominik Lorenz, Patrick Esser, and Björn Ommer. High-resolution image synthesis with latent diffusion models. In *Proceedings of the IEEE/CVF conference on computer vision and pattern recognition*, pages 10684–10695, 2022. 2
- [60] Olaf Ronneberger, Philipp Fischer, and Thomas Brox. U-net: Convolutional networks for biomedical image segmentation. In *Medical image computing and computer-assisted intervention—MICCAI 2015: 18th international conference, Munich, Germany, October 5-9, 2015, proceedings, part III 18*, pages 234–241. Springer, 2015. 2, 4
- [61] Olaf Ronneberger, Philipp Fischer, and Thomas Brox. U-net: Convolutional networks for biomedical image segmentation. In *Medical Image Computing and Computer-Assisted Intervention – MICCAI 2015*, pages 234–241, Cham, 2015. Springer International Publishing. 4
- [62] Jean-Michel Roufousse, Abhishek Sharma, and Maks Ovsjanikov. Unsupervised deep learning for structured shape matching. In *Proceedings of the IEEE/CVF International Conference on Computer Vision*, pages 1617–1627, 2019. 2
- [63] Raif M Rustamov. Laplace-beltrami eigenfunctions for deformation invariant shape representation. In *Eurographics Symposium on Geometry Processing*, 2007. 1, 3
- [64] Marcel Seelbach Benkner, Zorah Löhner, Vladislav Golyanik, Christof Wunderlich, Christian Theobalt, and Michael Moeller. Q-match: Iterative shape matching via quantum annealing. In *International Conference on Computer Vision (ICCV)*, 2021. 1
- [65] Nicholas Sharp, Souhaib Attaiki, Keenan Crane, and Maks Ovsjanikov. Diffusionnet: Discretization agnostic learning on surfaces. *ACM Transactions on Graphics (TOG)*, 41(3):1–16, 2022. 2, 7
- [66] Jascha Sohl-Dickstein, Eric Weiss, Niru Maheswaranathan, and Surya Ganguli. Deep unsupervised learning using nonequilibrium thermodynamics. In *International Conference on Machine Learning*, 2015. 1, 2, 4
- [67] Yang Song and Stefano Ermon. Generative modeling by estimating gradients of the data distribution. *Advances in neural information processing systems*, 32, 2019. 1, 2
- [68] Robert W Sumner and Jovan Popović. Deformation transfer for triangle meshes. *ACM Transactions on graphics (TOG)*, 23(3):399–405, 2004. 1
- [69] Mingze Sun, Shiwei Mao, Puhua Jiang, Maks Ovsjanikov, and Ruqi Huang. Spatially and spectrally consistent deep functional maps. In *International Conference on Computer Vision*, 2023. 1, 7, 8, 9, 17
- [70] Ramana Sundararaman, Gautam Pai, and Maks Ovsjanikov. Implicit field supervision for robust non-rigid shape matching. In *European Conference on Computer Vision*, pages 344–362. Springer, 2022. 2
- [71] Federico Tombari, Samuele Salti, and Luigi Di Stefano. Unique signatures of histograms for local surface description. In *European Conference on Computer Vision (ECCV)*, pages 356–369, 2010. 2
- [72] Giovanni Trappolini, Luca Cosmo, Luca Moschella, Riccardo Marin, Simone Melzi, and Emanuele Rodolà. Shape registration in the time of transformers. *Advances in Neural Information Processing Systems*, 34, 2021. 2, 4, 7
- [73] Gul Varol, Javier Romero, Xavier Martin, Naureen Mahmood, Michael J Black, Ivan Laptev, and Cordelia Schmid. Learning from synthetic humans. In *Proceedings of the IEEE conference on computer vision and pattern recognition*, pages 109–117, 2017. 2, 6
- [74] Patrick von Platen, Suraj Patil, Anton Lozhkov, Pedro Cuenca, Nathan Lambert, Kashif Rasul, Mishig Davaadorj, Dhruv Nair, Sayak Paul, William Berman, Yiyi Xu, Steven Liu, and Thomas Wolf. Diffusers: State-of-the-art diffusion models. <https://github.com/huggingface/diffusers>, 2022. 6
- [75] Lilian Weng. What are diffusion models? lilianweng.github.io, 2021. 6
- [76] Yiming Zeng, Yue Qian, Zhiyu Zhu, Junhui Hou, Hui Yuan, and Ying He. Cornnet3d: Unsupervised end-to-end learning of dense correspondence for 3d point clouds. In *Proceedings of the IEEE/CVF Conference on Computer Vision and Pattern Recognition*, pages 6052–6061, 2021. 2
- [77] Silvia Zuffi, Angjoo Kanazawa, David W Jacobs, and Michael J Black. 3d menagerie: Modeling the 3d shape and pose of animals. In *Computer Vision and Pattern Recognition (CVPR)*, pages 6365–6373, 2017. 8

Denoising Functional Maps: Diffusion Models for Shape Correspondence

Supplementary Material

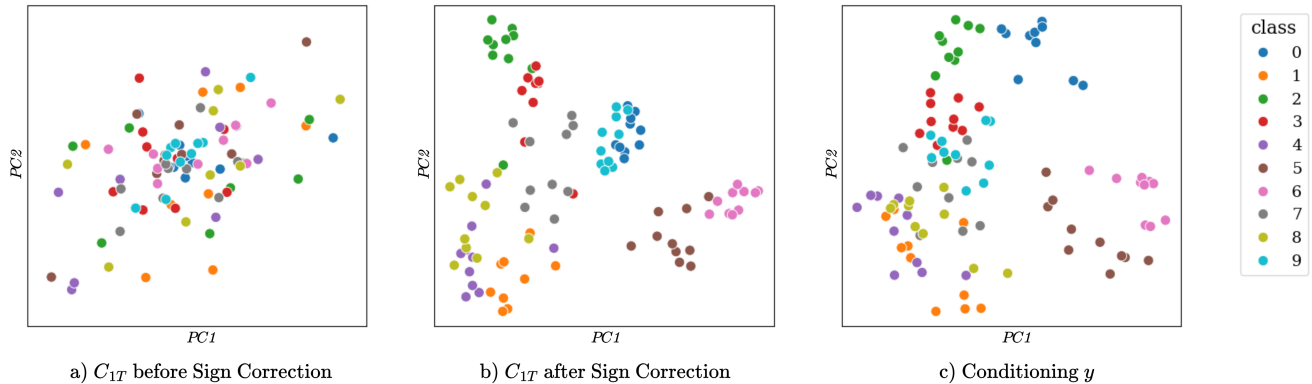


Figure 4. For the FAUST [7] dataset, we plot the first two PCA components for: a) the functional maps between each shape and the template before sign correction, b) the functional maps after sign correction, c) the projection matrix after sign correction. Each entry is colored according to its shape class. Note the clusters that form for the functional maps and projection matrices after sign correction.

# Ev	F_r	S_r	S'19_r	F_a	S_a
32	98.8	99.3	98.9	98.7	99.0
64	98.7	97.9	98.1	98.2	97.8
96	98.7	94.9	96.3	95.1	94.7

Table 5. Mean Sign Correction Accuracy in % for each evaluation dataset, averaged over 100 epochs.

This supplementary material presents several important components of our work that were not included in the main text:

- Evaluation of the sign correction network (Sec. A)
- Additional implementation details (Sec. B)
- A more thorough comparison with the baselines, ablation studies, and qualitative examples (Sec. C)
- Pseudocode of all algorithms (Sec. D)

A. Sign Correction

This section provides a quantitative and qualitative evaluation of the sign correction network. This component of our model allows to select a specific sign for eigenvectors of the Laplacian by projecting them onto the learned correction vector and making the projection positive (Sec. 4.2). After performing the sign correction on all eigenvectors, we obtain a specific basis, independent of the initial one provided by the numerical eigensolver.

A.1. Accuracy

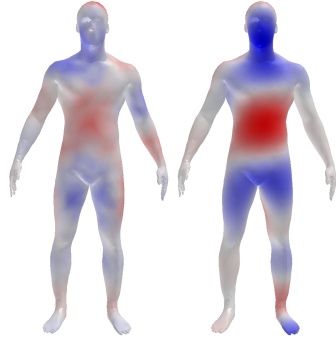
We first quantitatively evaluate the sign correction network on the human datasets considered in Sec. 5.2-5.3. We use a metric that we call the Mean Sign Correction Accuracy:

For each mesh, we calculate the 32, 64, and 96-dimensional eigenbasis twice, perform the sign correction (Eq. 4), and report the mean number of equal eigenvectors. The metric is averaged over 100 epochs for each dataset. The results are shown in Table 5: We observe that the trained sign corrector achieves a high accuracy of $>95\%$ on all datasets.

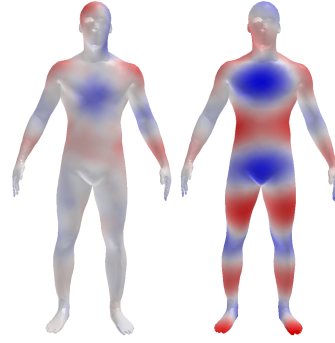
A.2. Distribution of Functional Maps

Here we study the change in the distribution of functional maps after sign correction. We use the FAUST [7] dataset, which contains meshes of 10 classes of humans with various body types in different poses. For each mesh, we obtain a 32-dimensional eigenbasis and correct it with a pretrained sign correction network. We then compute the template-wise functional maps, as well as the conditioning matrix y (Eq. 8).

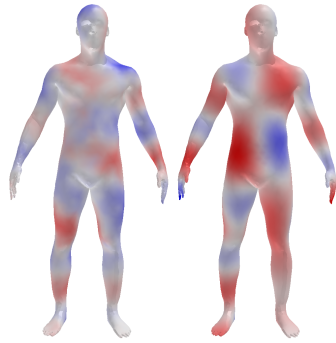
Next, we perform PCA decomposition [2] on the functional maps before and after sign correction, as well as on the conditioning matrix. The pairwise plots of the first two components are shown in Fig. 4, where each point is colored according to its class. As we can see, before sign correction, the functional maps did not have a sensible distribution since each of them was defined in a random basis. After the sign ambiguity was resolved, the functional maps form noticeable clusters grouped by class. For the conditioning matrix, the overall structure resembles the distribution of functional maps after sign correction. This explains the basic principle of our method: the sign correction network transformed the space of functional maps into a learnable distribution by making them refer to a specific basis, and the denoising diffusion model approximated this distribution.



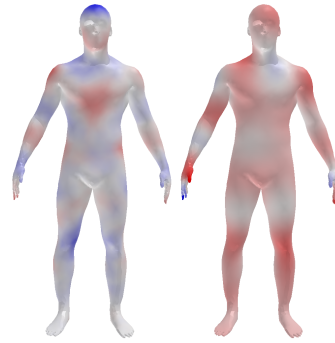
(a) Learned correction vector ς_{24} (left) and the corresponding eigenvector ϕ_{24} (right). The projection is 0.51, so we keep the sign of the eigenvector.



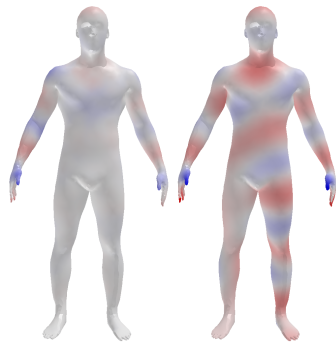
(b) Same for ς_{32} and ϕ_{32} . The projection is 0.24.



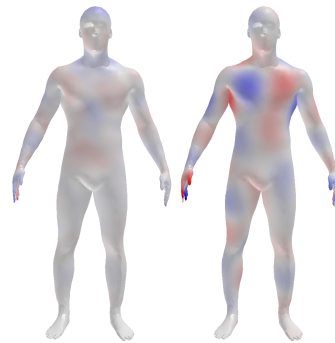
(c) Same for ς_{40} and ϕ_{40} . The projection is -0.18 , so the eigenvector should be multiplied by -1 .



(d) Same for ς_{48} and ϕ_{48} . The projection is -0.35 , so the eigenvector should be multiplied by -1 .



(e) Same for ς_{56} and ϕ_{56} . The projection is 0.69.



(f) Same for ς_{64} and ϕ_{64} . The projection is -0.29 , so the eigenvector should be multiplied by -1 . Note the weights on the left hand (from our point of view).

Figure 5. Learned correction vectors and their corresponding eigenvectors. Positive and negative values are shown in red and blue, respectively. The low-order correction vectors resemble the eigenvectors themselves, while the high-order ones are mainly concentrated in the arm and hand regions.

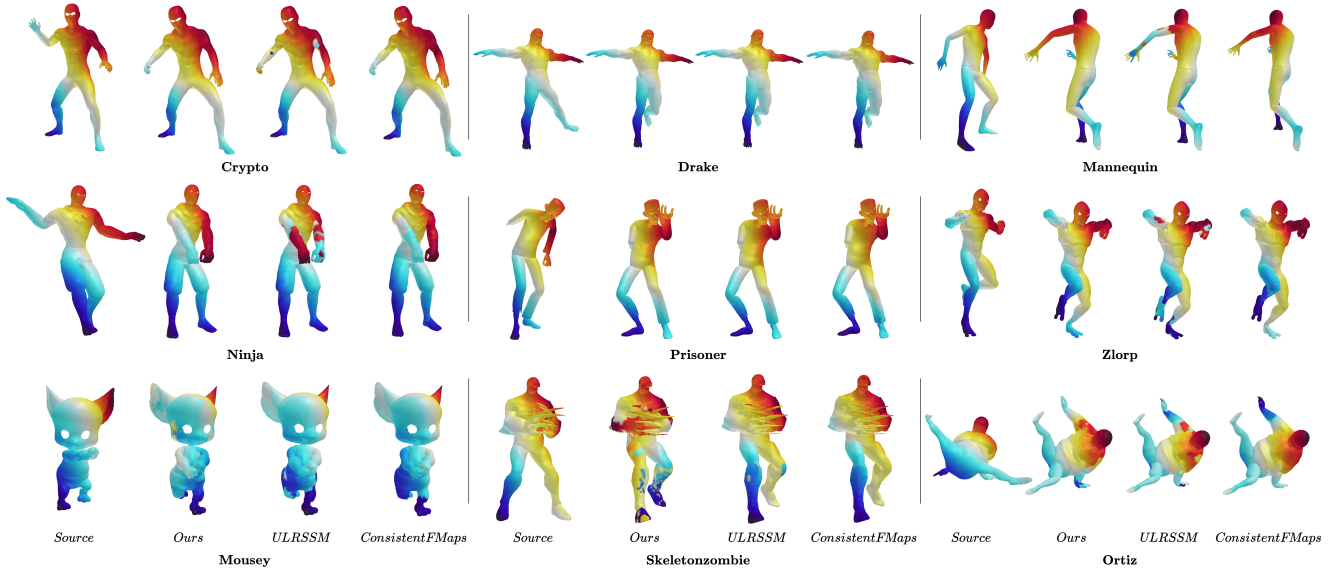
A.3. Learned Correction Vectors

We visualize several of the learned correction vectors in Fig. 5, along with the corresponding eigenvectors. As we can see, the low-order correction vectors resemble the

eigenvectors themselves, while the high-order ones are mostly concentrated in the arm and hand regions.



(a) Examples on human shapes from the FAUST, SCAPE, and SHREC'19 datasets.



(b) Examples on the DT4D intra-category dataset, compared to ULRSSM [11], a state-of-the-art descriptor-based approach. Our method outperforms it on most shape classes, except for a few categories that are too different from the training data: “Mousey”, “Skeletonzombie”, “Ortiz”. The correspondences for the “Drake” class are mostly correct but sometimes have flipped left-right symmetry.

Figure 6. Additional qualitative examples. Our method provides correct correspondences for many challenging human and humanoid meshes.

B. Additional Implementation Details

B.1. Robustness to Basis Ambiguity

To make the sign correction network applicable to high-order eigenvectors, we need to make it robust to possible basis ambiguity that arises when an eigenvalue has high multiplicity (see Sec. 3.2). Numerically, an eigenvalue with

multiplicity $d > 1$ is represented as d adjacent eigenvalues $\lambda_i \dots \lambda_{i+d}$ with close values.

A straightforward way to account for the basis ambiguity is to use a single correction vector ς_i for several adjacent eigenvectors instead of only one eigenvector ϕ_i . In practice, we split the eigenvectors into groups of 32 and select increasingly more eigenvectors per correction vector for each

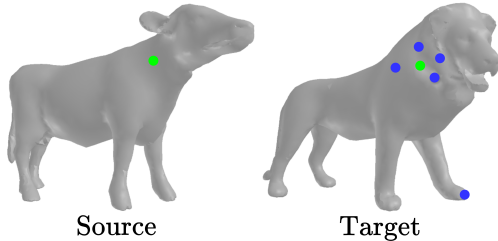


Figure 7. Illustration of the Dirichlet Medoid map selection. Given $k = 6$ candidate matches on the target shape, we report the one that has the lowest total distance to the other $k - 1$ candidates (shown in green).

group: one for $\phi_1 - \phi_{32}$, two for $\phi_{33} - \phi_{64}$, and two or four for $\phi_{65} - \phi_{96}$. This takes into account the fact that high-order eigenvalues are more likely to have high multiplicity.

B.2. Training the Sign Corrector

The training process described in Sec. 4.2.2 is based on correcting the signs of two sets of eigenvectors Φ_1 and Φ_2 on the mesh S , which can be obtained by performing eigendecomposition with a numerical solver twice. Due to the sign ambiguity, the difference between them can be written as $\Phi_2 = \Phi_1 \sigma$, where $\sigma \in \{-1, 1\}^n$ is the ground-truth sign difference. However, we do not need to perform the costly eigendecomposition at each training iteration. Instead, we can compute the eigenbasis Φ once, and during training randomly sample two sign combinations $\sigma_1, \sigma_2 \in \{-1, 1\}^n$ to obtain new basis combinations $\Phi_1 = \Phi \sigma_1, \Phi_2 = \Phi \sigma_2$. This significantly reduces the training time.

B.3. Map Selection

Here, we provide more details about our map selection step (Sec. 4.1.2). We repeat the denoising process n times and rank the candidate maps based on their Dirichlet energy (i.e. map smoothness). If we simply report the map with the lowest Dirichlet energy, it may be prone to outliers such as smooth maps with flipped left-right symmetry. To address this, we select k maps with the lowest Dirichlet energy and iterate over each point on the source shape to combine them. At each step, we have k candidate matching points on the target shape, potentially containing outliers.

We find the *medoid* match (the one that has the lowest total distance to the other $k - 1$ candidates) and report it; see Fig. 7 for an illustration. After repeating these steps for each point on the source shape, we construct a map that we call the ‘‘Dirichlet Medoid’’. In practice, we sample a total of $n = 128$ raw maps and use $k = 16$ for the medoid selection.

Test	F.r	S.r	S’19.r
GeomFMaps	1.9	2.4	7.5
ConsistentFMaps	2.2	2.3	4.3
DiffZO	1.9	2.2	3.6
ULRSSM	1.6	2.1	4.6
SSL	2.0	3.1	4.0
SmS (with align.)	2.7	2.5	3.2
SmS (no align.)	3.4	3.2	4.0
Ours – 64×64	1.8	2.3	3.5
Ours – 96×96	1.7	2.1	3.6

Table 6. Comparison with descriptor-based methods trained on FAUST+SCAPE. The **best** and **2nd best** results are highlighted. SmS [12] requires rigid pre-alignment of training and test shapes to the same orientation, so we evaluated it on both aligned and unaligned datasets. Note that our method is fully intrinsic and insensitive to rigid orientation.

C. Additional Evaluation

C.1. PCK Curves

We show PCK curves for the FAUST, SCAPE, and SHREC’19 datasets in Fig. 8, which plot the percentage of correctly predicted keypoints within different distance thresholds from the ground truth. Our method demonstrates competitive performance compared to ULRSSM [11] and AttentiveFMaps [33].

C.2. Qualitative Examples

Fig. 6a shows qualitative examples of correspondences obtained by our method on FAUST, SCAPE, and SHREC’19 datasets. Fig. 6b qualitatively compares our model with two baselines on all shape classes from the DT4D dataset. Our method obtains smooth and accurate correspondences for human-like shapes with diverse body types and poses, but it is not as accurate on classes that are too different from the training data.

C.3. Baselines Trained on FAUST and SCAPE

In Sec. 5.2, we evaluated descriptor-based methods that were trained on the FAUST dataset since it contains diverse SMPL-like shapes, while SCAPE is too small to fine-tune large models. For a complete comparison, here we additionally evaluate baselines trained on both FAUST and SCAPE. The results are shown in Table 6. As we can see, our method still performs *on par* with state-of-the-art methods, even without additional variety provided by the shapes from SCAPE.

C.4. Baselines Trained on SURREAL

Here, we study the performance of other functional map-based methods with respect to dataset size. We trained several baselines on 5,000 randomly selected shapes from SURREAL and evaluated them. As shown in Table 7, the

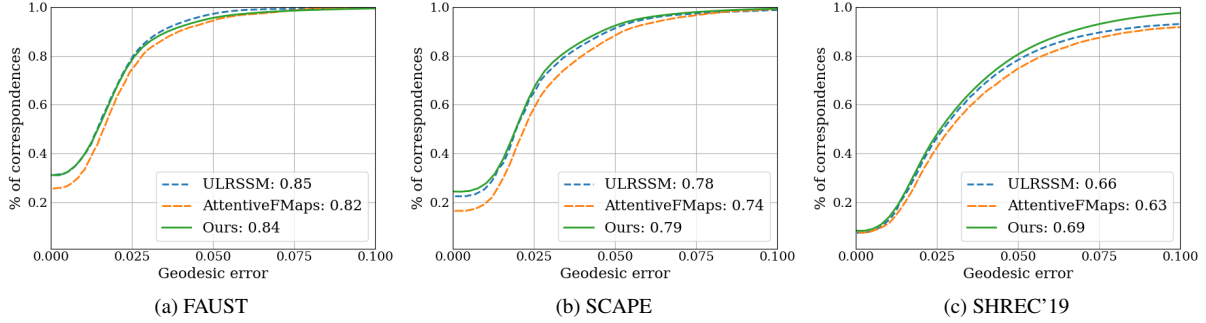


Figure 8. PCK curves for the evaluation datasets. Our method demonstrates superior or similar performance compared to existing approaches.

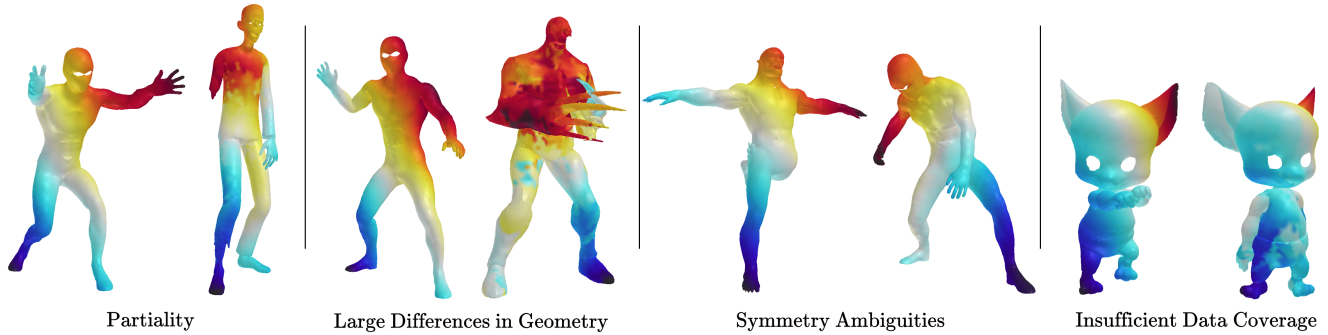


Figure 9. Limitations of our method. They include shapes with large differences from the synthetic human data, as well as topological inconsistencies like missing body parts. These limitations may be addressed in future work.

Test	F	S	S'19
GeomFMaps	1.9	2.5 \uparrow	7.1 \downarrow
ULRSSM	1.6	2.5 \uparrow	4.8 \uparrow
SSL	2.0	3.2 \uparrow	4.4 \uparrow

Table 7. Results of descriptor-based methods trained on 5,000 shapes from SURREAL. Arrows indicate the change in error compared to FAUST+SCAPE (see Table 6).

large dataset size negatively impacts the performance of previous works, with slightly worse results compared to training on FAUST and SCAPE.

Additionally, we note that DiffusionNet-based methods require storing the full decomposition of the Laplacian, which does not scale well to large datasets. For the full SURREAL dataset, this would require about 1 TB of space. Instead, our model only stores the conditioning matrices and the functional maps, which takes at most 24 GB.

C.5. Impact of ZoomOut

To illustrate the role that ZoomOut refinement [44] plays in our pipeline, we tested our models without the spectral upsampling step. The results are shown in Tables 8a and 8b. As we can see, ZoomOut plays a key role for 32×32

	64×64		96×96	
	no ZO	Ours	no ZO	Ours
F	2.0	1.8	1.8	1.7
S	2.6	2.3	2.2	2.1
S19	4.1	3.5	3.9	3.6

(a) Results on FAUST, SCAPE, and SHREC'19 datasets.

	32×32	
	no ZO	Ours
manneq.	2.0	1.0
zlorp	2.2	1.1
crypto	2.3	1.1
prisoner	3.9	1.1
ninja	2.7	1.4
ortiz	19.5	9.3
mousey	18.1	10.2
drake	12.5	10.6
skeletonz.	33.2	16.3

(b) Results on the DT4D dataset.

Table 8. Results of our models with and without ZoomOut [44] refinement.

and 64×64 models, while it is less important for the 96×96 model.

Class	Intra			Inter		
	32	64	96	32	64	96
manneq.	1.0	1.0	1.0	3.3	3.2	3.2
zlorp	1.1	1.1	1.1	4.2	3.6	4.4
crypto	1.1	1.1	1.0	–	–	–
prisoner	1.1	2.3	9.1	29.6	28.1	34.5
ninja	1.4	2.0	9.3	4.3	5.2	9.5
ortiz	9.3	17.0	24.2	–	–	–
mousey	10.2	17.9	25.6	–	–	–
drake	10.6	6.8	9.4	10.4	8.5	13.2
skeletonz.	16.3	30.1	36.5	49.4	31.5	39.3

Table 9. Results of our 32×32, 64×64, and 96×96 models on shape classes from DT4D-H.

Ablation Setting	SHREC’19
w/o basis ambiguity (Sec. B.1)	5.8
w/o ZoomOut	4.1
w/o any map selection (Sec. 4.1.2)	4.7
w/o medoid map selection (Sec. B.3)	3.7
Ours	3.5

Table 10. Ablation study of the 64×64 model on SHREC’19.

C.6. DT4D: Impact of the Model Dimension

Our previous experiments show that models predicting high-dimensional functional maps achieve higher accuracy, while low-dimensional ones provide better generalization to unseen shape classes. To illustrate this, we show in Table 9 the results of all our models on shape classes from DT4D. As we can see, the 32×32 model achieves excellent performance on most shape classes, while the 96×96 one shows high accuracy on a few specific classes but fails on others. The 64×64 model falls in between.

C.7. Ablation Study

Next, we ablate different parts of our method. We use a 64×64 model and the SHREC’19 dataset since it provides the largest shape diversity; see Table 10 for the results. As we can see, addressing the basis ambiguity (Sec. B.1) is crucial for the matching performance. Second, using ZoomOut [44] to increase the resolution of the functional map helps to improve the accuracy. Finally, using map selection criteria based on Dirichlet energy is also a necessary component of our model, and selecting the medoid among several smoothest maps (rather than using the map with the lowest Dirichlet Energy) helps to filter out the outliers.

C.8. Comparison with ULRSSM on DT4D

In Sec. 5.4, we evaluated our method on shape classes from the DT4D dataset against the baselines, ConsistentFMaps [69] and ULRSSM [11]. Compared to other descriptor-based methods, ULRSSM fine-tunes the parameters of the feature extractor by backpropagating the unsupervised loss

Class	Intra			Inter		
	Ours	[11] FT	[11] no FT	Ours	[11] FT	[11] no FT
manneq.	1.0	1.0	3.4	3.3	4.0	11.3
zlorp	1.1	1.3	5.2	4.2	6.9	21.3
crypto	1.1	1.5	3.3	–	–	–
prisoner	1.1	1.1	1.4	29.6	20.5	33.0
ninja	1.4	5.6	11.7	4.3	16.2	30.6
ortiz	9.3	4.4	7.8	–	–	–
mousey	10.2	2.7	5.2	–	–	–
drake	10.6	1.0	2.6	10.4	8.2	26.4
skeletonz.	16.3	1.4	4.7	49.4	36.5	55.1

Table 11. Results of our method on shape classes from DT4D [40] compared to ULRSSM [11] with and without fine-tuning.

during test time for each evaluation pair. For a complete comparison, we evaluate ULRSSM without refinement, which leads to worse results of this baseline; see Table 11.

C.9. Limitations

In Fig. 9, we illustrate the main limitations of our method. These include shapes with significant differences from the synthetic human data we used for training, as well as shapes with missing body parts. In these cases, our method tends to output maps with incorrect left-right symmetry. These limitations may be addressed in future work.

D. Algorithms

We additionally provide the algorithms discussed in Sec. 4 as pseudocode. The training and inference of the diffusion model are described in Alg. 1 and Alg. 2, respectively. The sign correction is described in Alg. 3 and the training process in Alg. 4.

Algorithm 1: DDPM Training Pipeline

- 1 Train the Sign Correction Network Θ ;
 - 2 Correct all eigenvectors Φ with Θ in the dataset;
 - 3 Get functional maps to the template, C_{1T} ;
 - 4 Calculate conditioning y ;
 - 5 Train a DDPM to predict C_{1T} given y ;
-

Algorithm 2: DDPM Inference with Selection

Input: Shape collection $\{S_i\}$, List of Test Pairs \mathcal{L} ,
Sign Correction Net Θ , DDPM

```
// Template Stage
1 for shape  $S$ , eigenvectors  $\Phi$  in  $\{S_i\}$  do
2   repeat  $n = 128$  times // See 4.1.2
3   |   Correct the signs of  $\Phi$ , get conditioning  $y$ ;
4   |    $C_{1T} := \mathbf{DDPM}(y)$ ;
5   |   Convert  $C_{1T}$  to pointwise map  $\Pi_{T1}$ ;
6 end

// Pairwise Stage
7 for shapes  $S_1, S_2$  in  $\mathcal{L}$  do
8    $\mathcal{T}_\Pi := \{\}$ ;
9   repeat  $n = 128$  times // See 4.1.2
10  |    $C_{12} := \mathbf{LstSq}(\Pi_{T2}\Phi_2, \Pi_{T1}\Phi_1)$ ;
11  |   Zoomout  $C_{12}$  to  $[200, 200]$ ;
12  |   Convert  $C_{12}$  to pointwise map  $\Pi_{21}$ ;
13  |   Add  $\Pi_{21}$  to  $\mathcal{T}_\Pi$ ;
14   $\hat{\Pi}_{21} := \mathbf{Selection}(\mathcal{T}_\Pi)$ 
15 end

Output: pointwise maps  $\hat{\Pi}_{21}$  for each pair
```

Algorithm 3: Learned Sign Correction

Input: Shape S , eigenvectors $\Phi \sim (v, n)$,
vertex-area matrix $A \sim (v, v)$, feature
extractor Θ

```
1  $\Sigma := \Theta(S)$ ; // See B.1,  $(v, n)$ 
2  $P := \Sigma^T A \Phi$ ; //  $(n, n)$ 
3 if training then
4 |  $\hat{\sigma} := \mathbf{Diag}(P)$ ; //  $(n)$ 
5 else
6 |  $\hat{\sigma} := \mathbf{Sign}(\mathbf{Diag}(P))$ ; //  $(n)$ 
7 end
8  $\hat{\Phi} := \Phi \hat{\sigma}$ ; //  $(v, n)$ 
```

Output: Eigenvectors with corrected signs $\hat{\Phi}$,
correcting sign sequence $\hat{\sigma}$

Algorithm 4: Unsupervised Training of Sign Correction

Input: Shape collection $\{S_i\}$, feature extractor Θ

```
1 for  $N$  epochs do
2   for shape  $S$ , eigenvectors  $\Phi$  in  $\{S_i\}$  do
3     // -1 or 1
4      $\sigma_1 := \mathbf{RandomSigns}(n)$ ;
5      $\sigma_2 := \mathbf{RandomSigns}(n)$ ;
6      $\Phi_1 := \Phi \sigma_1$ ;
7      $\Phi_2 := \Phi \sigma_2$ ;
8     // Alg. 3
9      $\hat{\sigma}_1 := \mathbf{SignCorr}(S, \Phi_1, \Theta)$ ;
10     $\hat{\sigma}_2 := \mathbf{SignCorr}(S, \Phi_2, \Theta)$ ;
11     $\mathcal{L}_{\text{sign}} := \mathbf{MSE}(\sigma_1 \sigma_2, \hat{\sigma}_1 \hat{\sigma}_2)$ ;
12     $\mathbf{Backpropagate}(\mathcal{L}_{\text{sign}})$ 
13  end
14 end
```

Output: Trained feature extractor $\hat{\Theta}$
